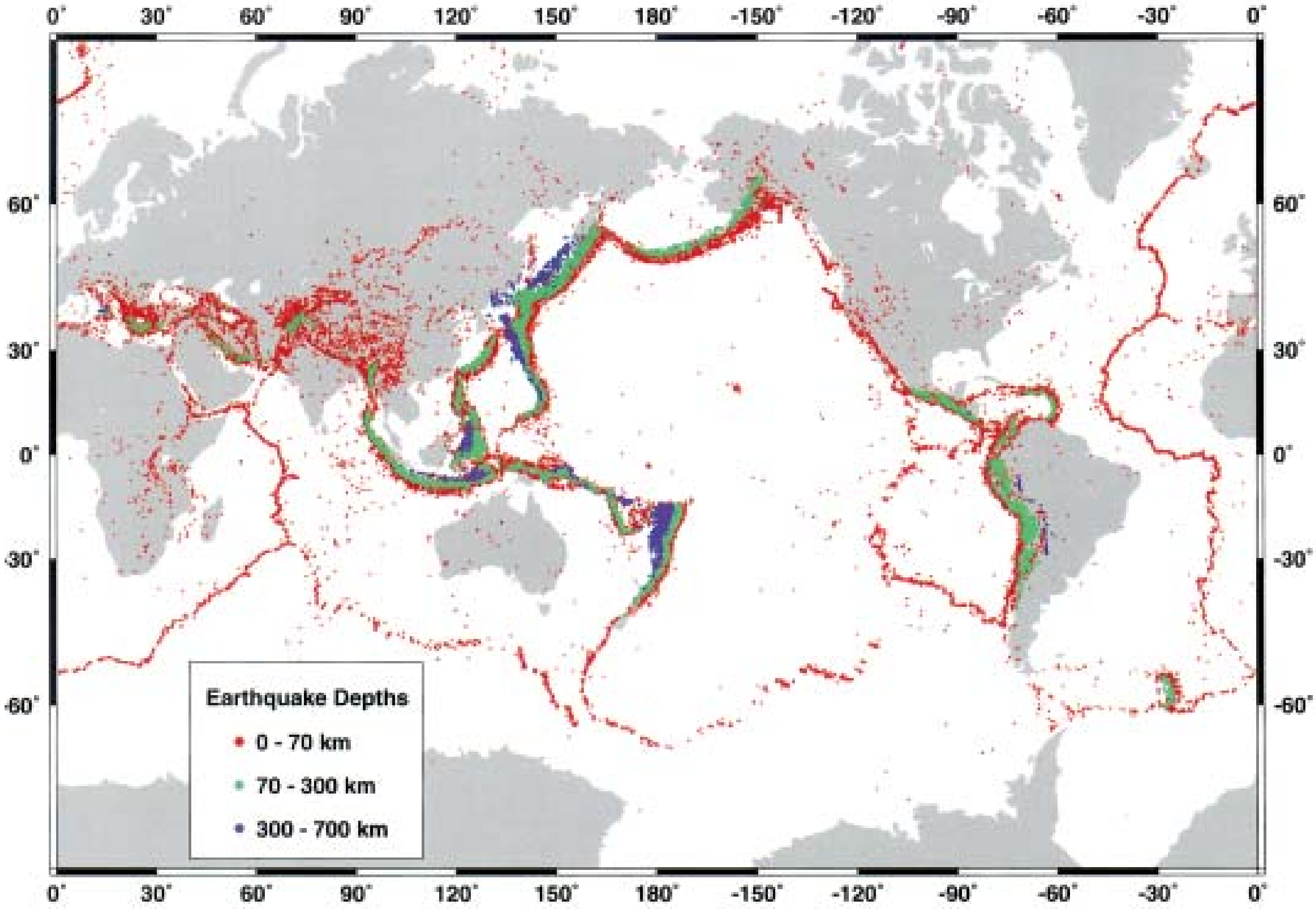

Figure 2.2. The global distribution of both shallow and deep seismicity for well-located earthquakes with magnitude > 5.1. The shallow seismicity closely delineates plate boundaries. Based on Engdahl et al. (1998).

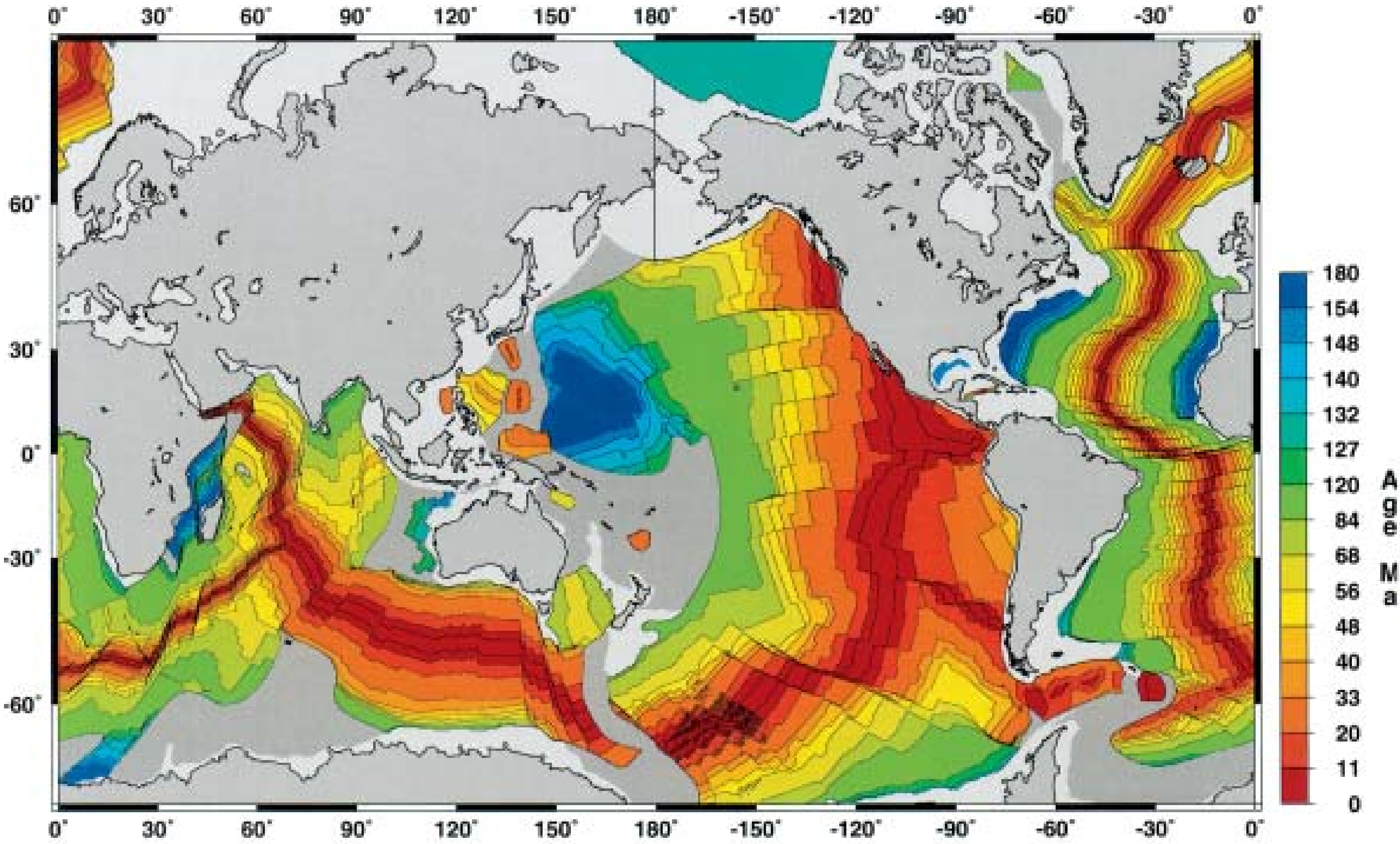

Figure 2.3. Age distribution of the oceanic crust as determined by magnetic anomalies on the seafloor. Based on Mueller et al. (1997).

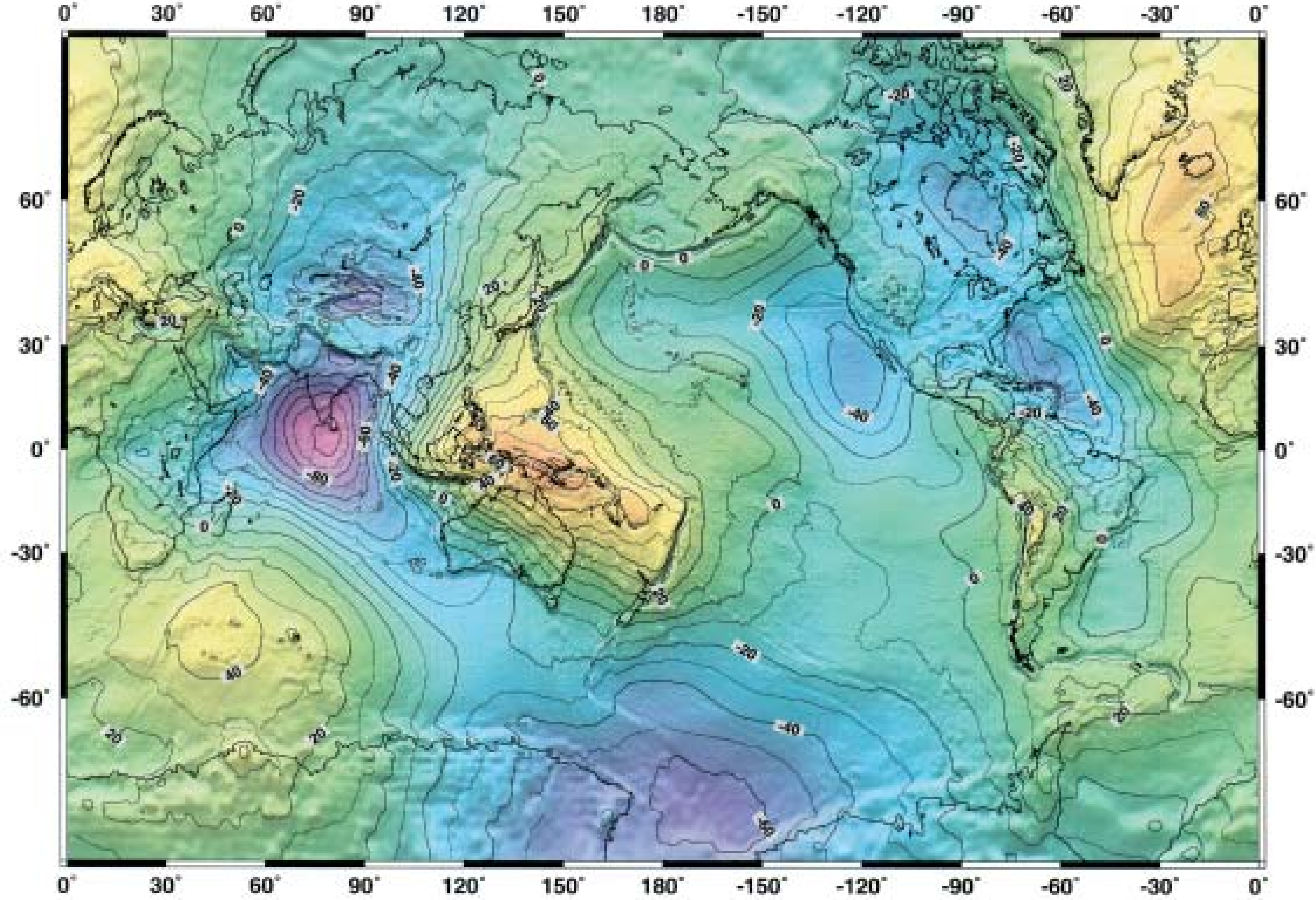

Figure 2.4. (a) Global geoid variations (after Lemoine et al., 1998). (a) is model EGM96 with respect to the reference ellipsoid WG584.

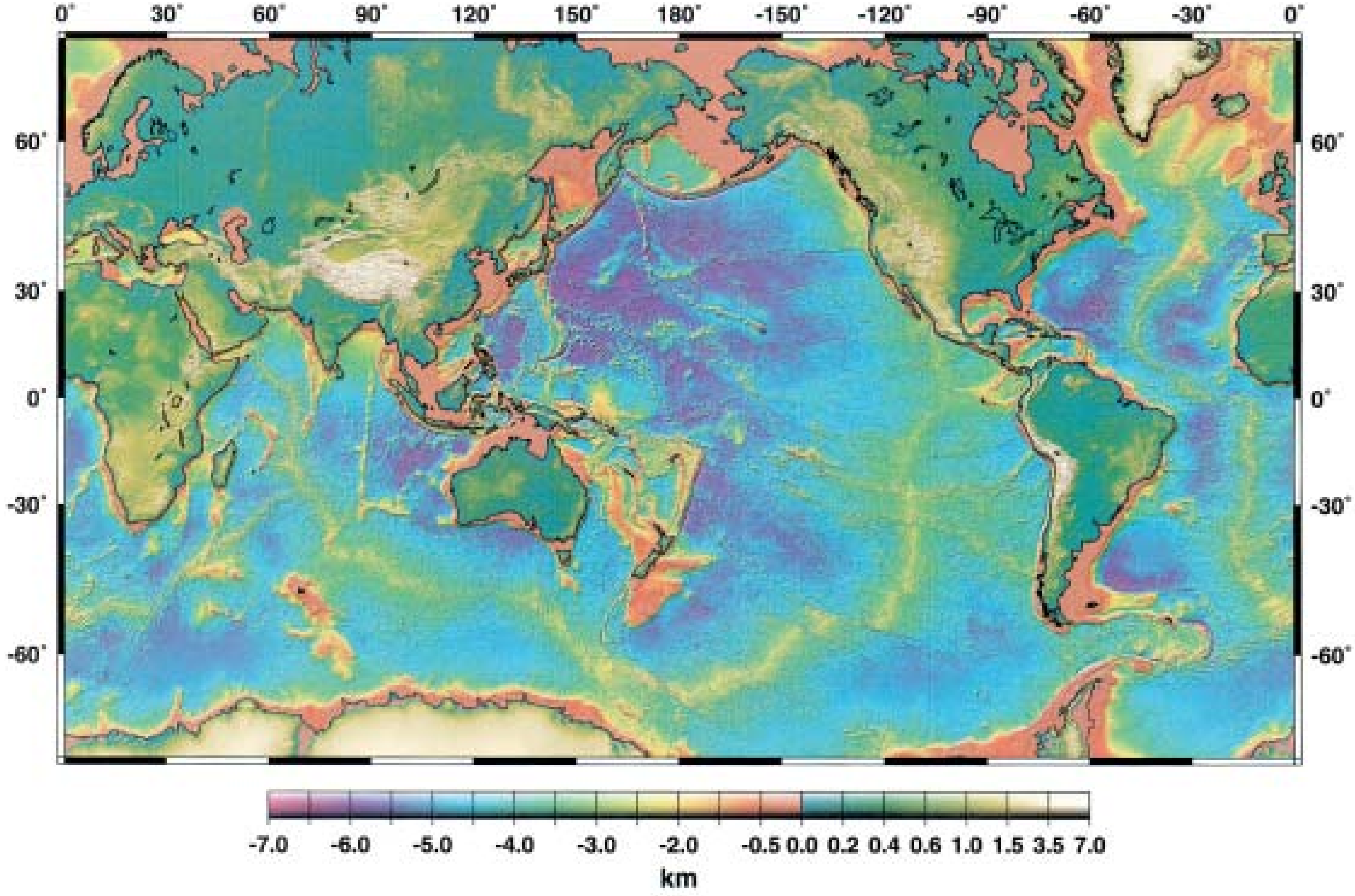

Figure 2.7. Global topography. The mountain range on the seafloor, the system of mid-ocean ridges, is a prominent feature of the Earth’s topography. Based on Smith and Sandwell (1997).

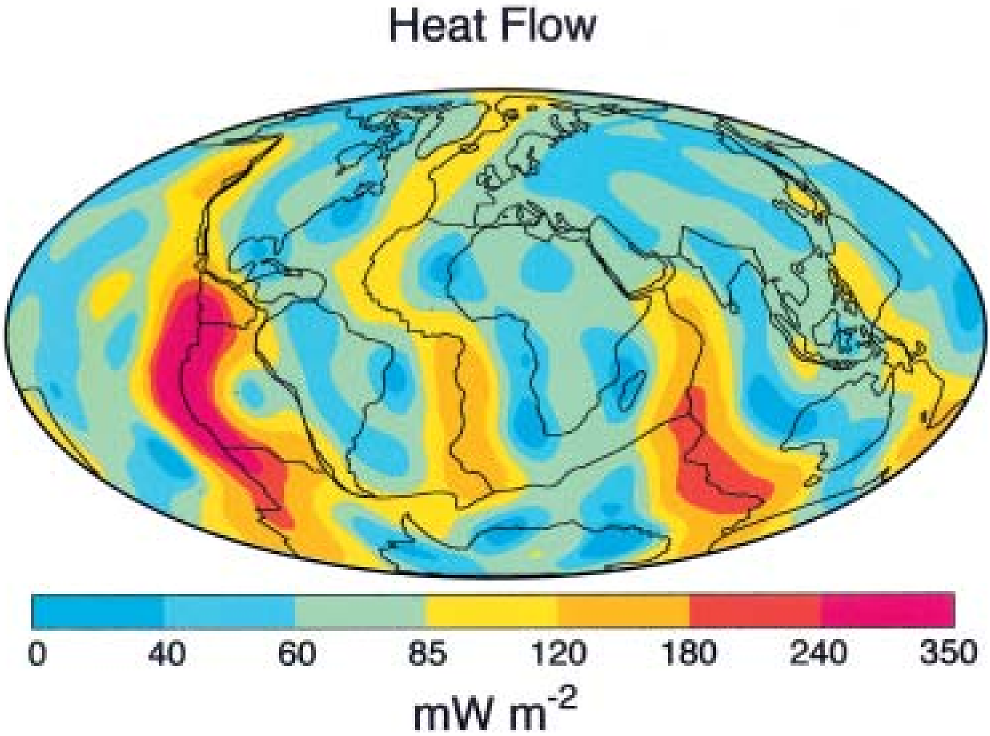

Figure 2.8. Pattern of global heat flux variations complete to spherical harmonic degree 12. After Pollack et al. (1993).

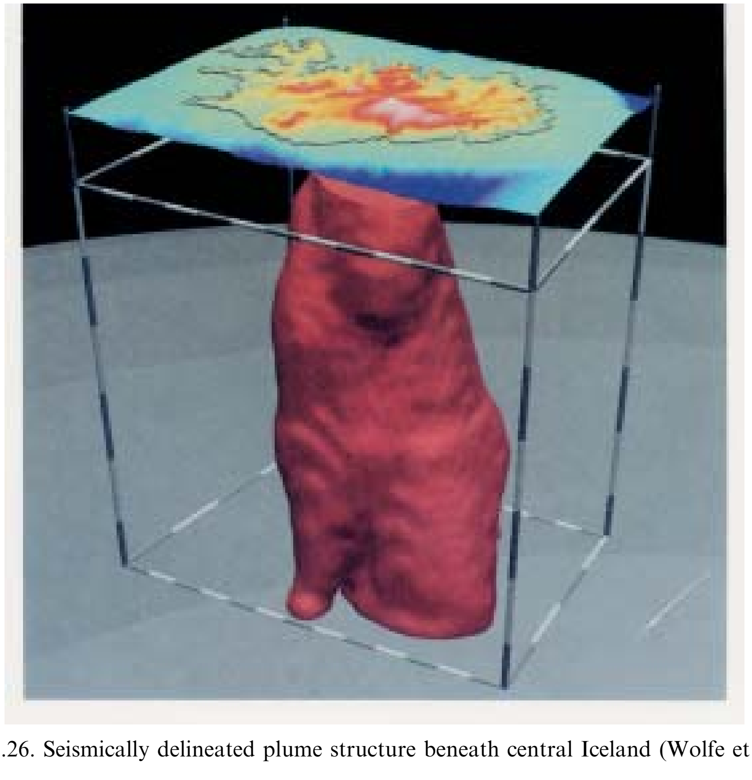

Figure 2.26. Seismically delineated plume structure beneath central Iceland (Wolfe et al., 1997).

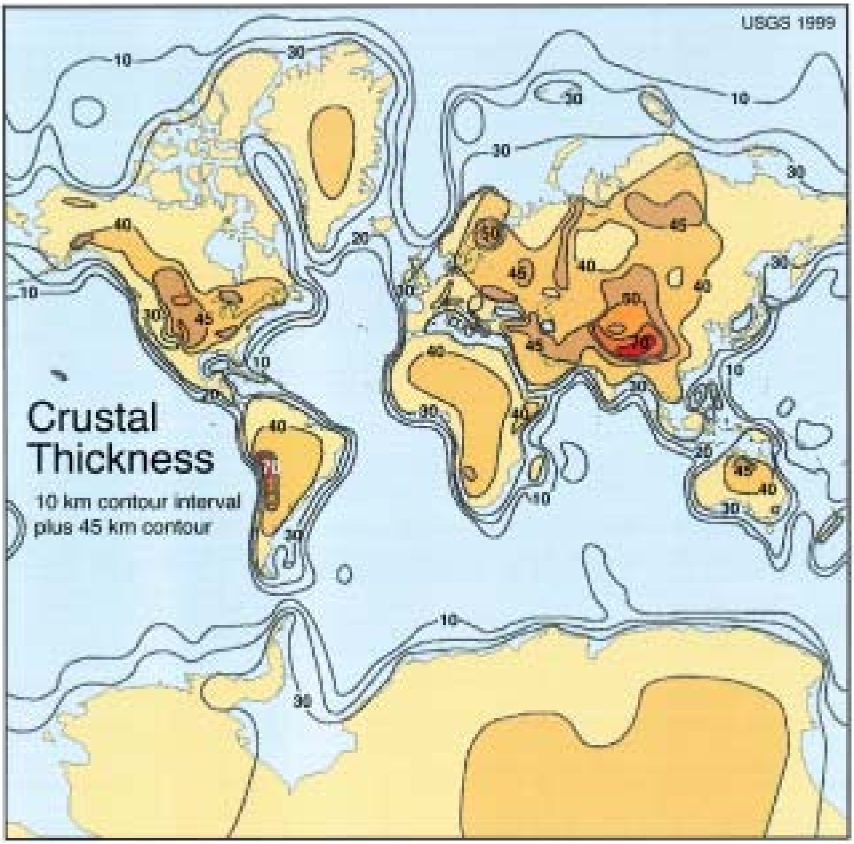

Figure 3.8. Global map of the thickness of the Earth's crust from the CRUST 5.1 model of Mooney et al. (1998). Crust thickness includes topography above sea level but not bathymetry.

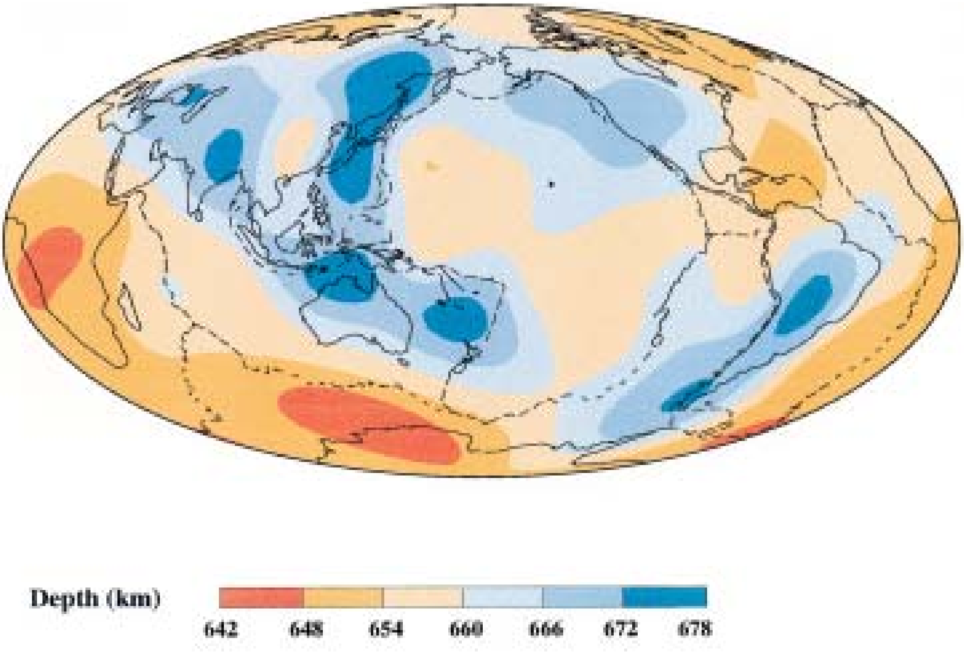

Figure 3.17. Depth of the 660 km seismic discontinuity. After Flanagan and Shearer (1998a).

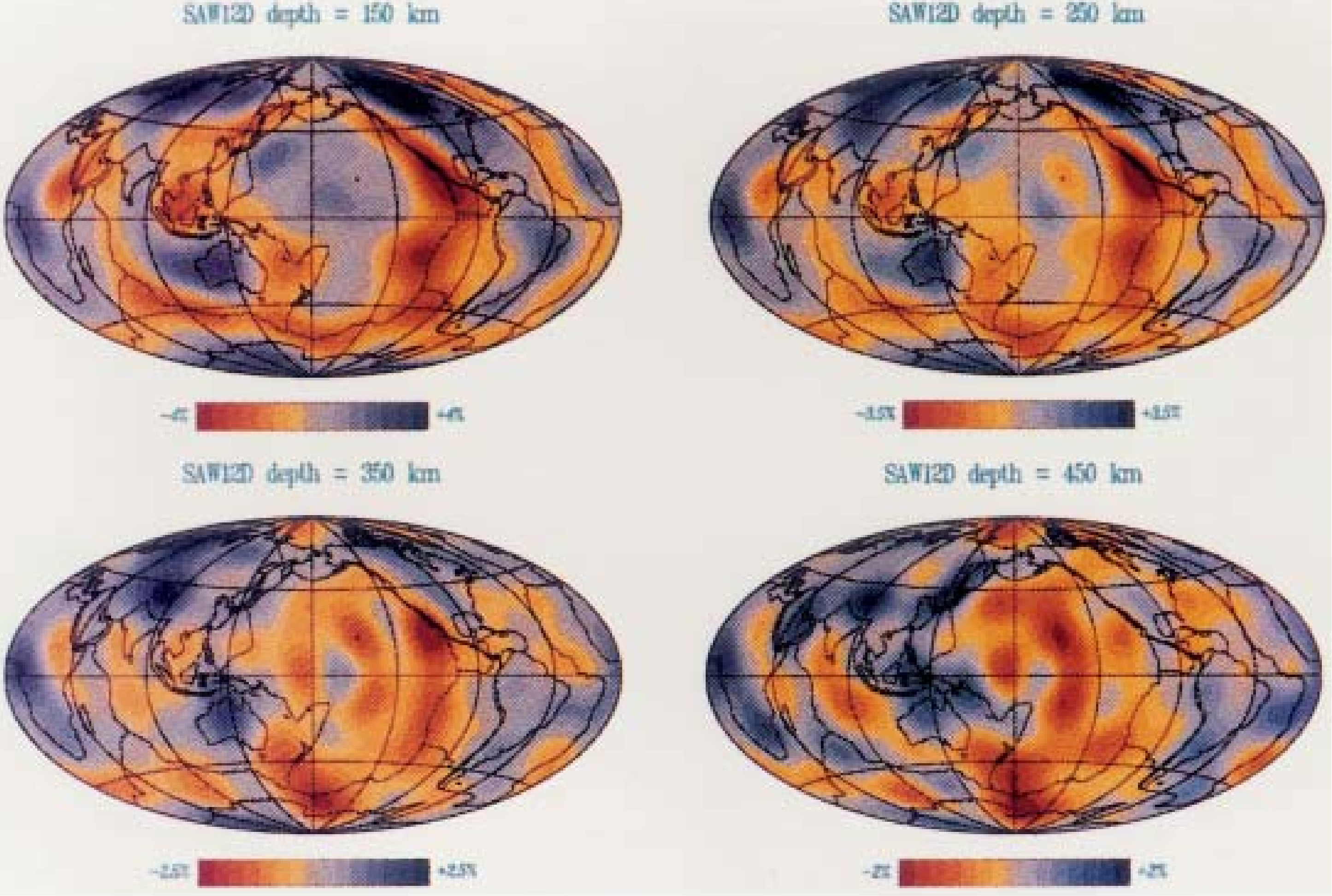

Figure 3.24. Perturbations in shear wave velocity V_S relative to the spherical Earth model PREM at various upper mantle depths from the model of Li and Romanowicz (1996).

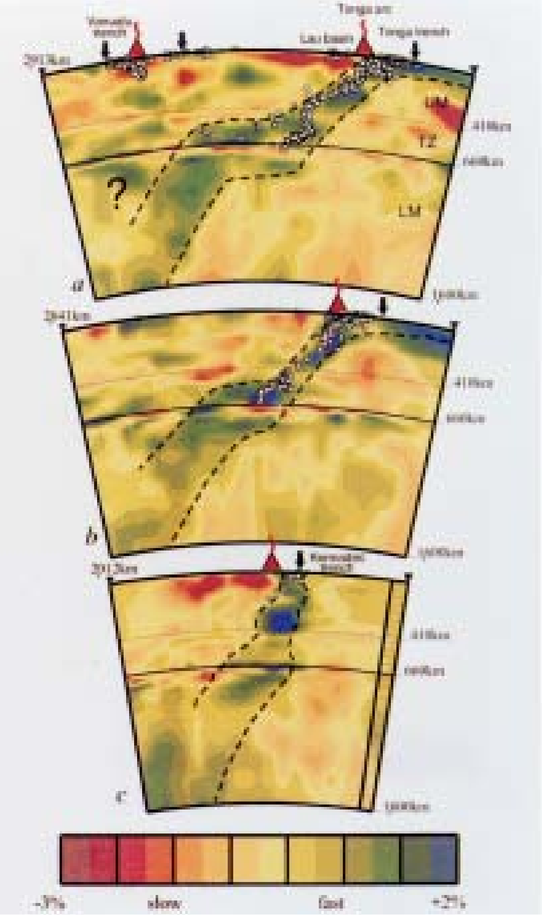

Figure 3.27. Tomographic images of seismic wave velocity V_P variations in the mantle beneath (a) the northern portion of the Tonga trench, (b) central Tonga, and (c) the Kermadec trench. Dots indicate earthquake foci. From van der Hilst (1995).

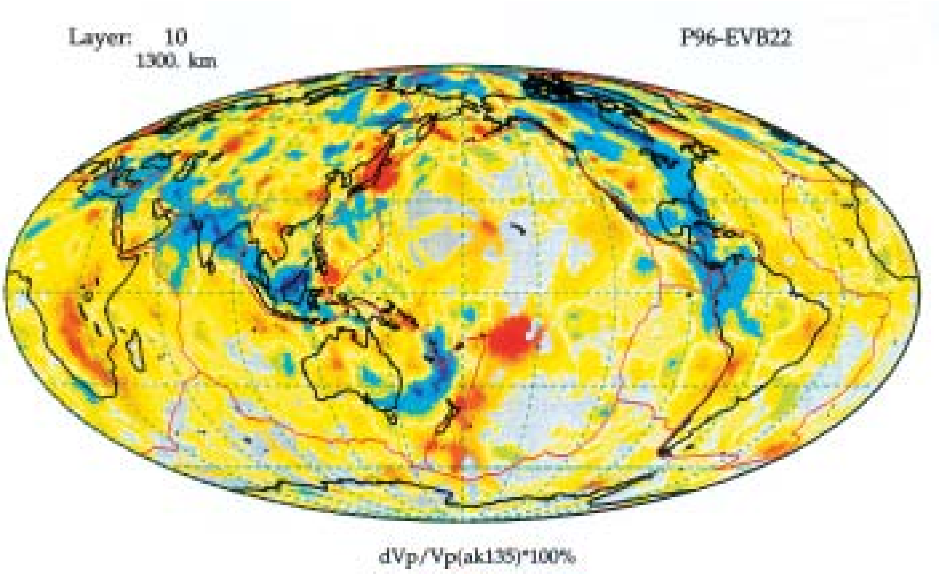

Figure 3.28. Perturbations in compressional wave velocity V_P relative to the spherical Earth model PREM at a depth of 1,300 km from the tomography model of Widiyantoro and van der Hilst (1996).

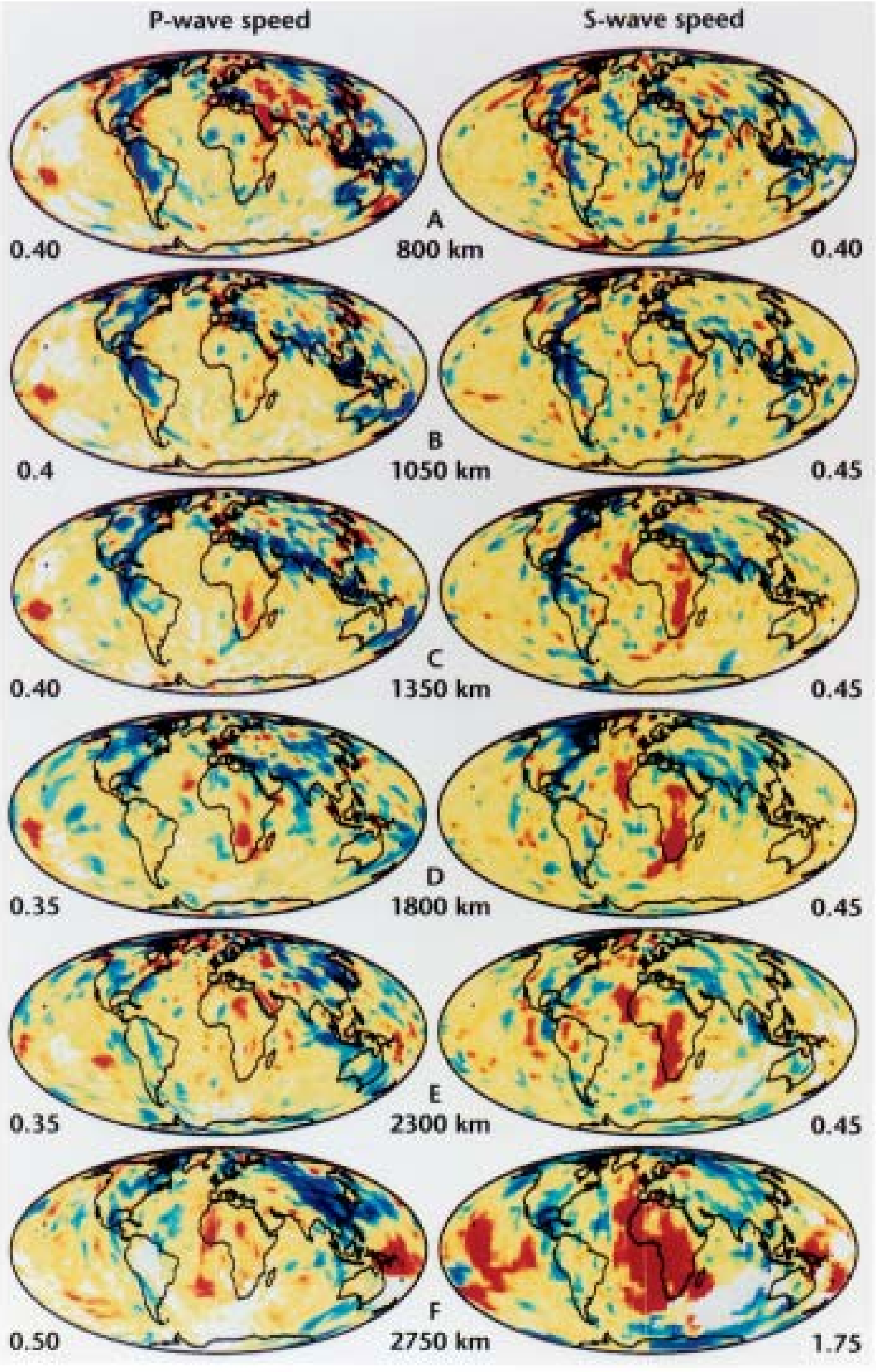

Figure 3.30. High-resolution P-wave and S-wave tomographic models of the lower mantle. Numbers at the sides of the images are the maximum anomaly in terms of percentage difference from the mean velocity. Blues are faster than average speed, reds are slower. White regions have no significant data sampling. After Grand et al. (1997).

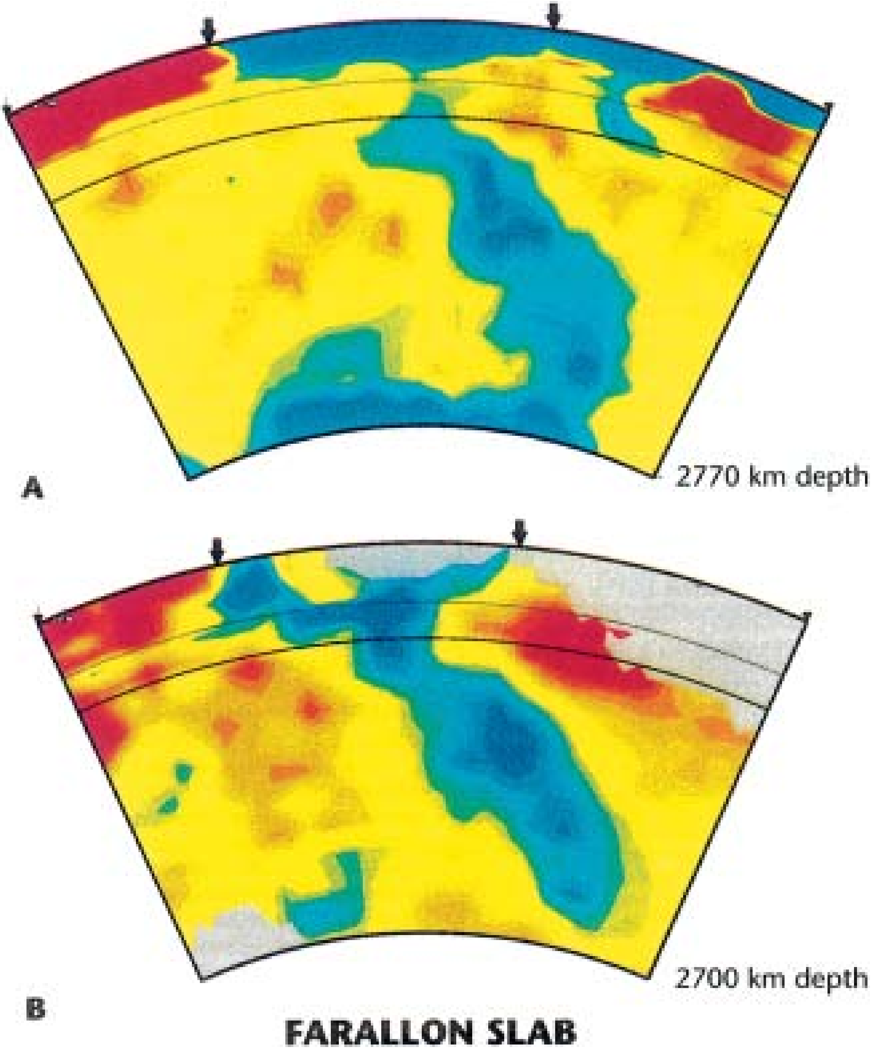

Figure 3.31. P- (A) and S- (B) wave velocity anomalies (relative to the global mean) at depths from the surface to the CMB in an approximately E–W cross-section of the mantle through the southern U.S. Reds indicate slow velocities, blues fast velocities. Differences in structure between the P-wave and S-wave models in the transition zone and near the CMB may be due to different data sampling in the two studies. The thin black lines are at depths of 410 and 660 km. After Grand et al. (1997).

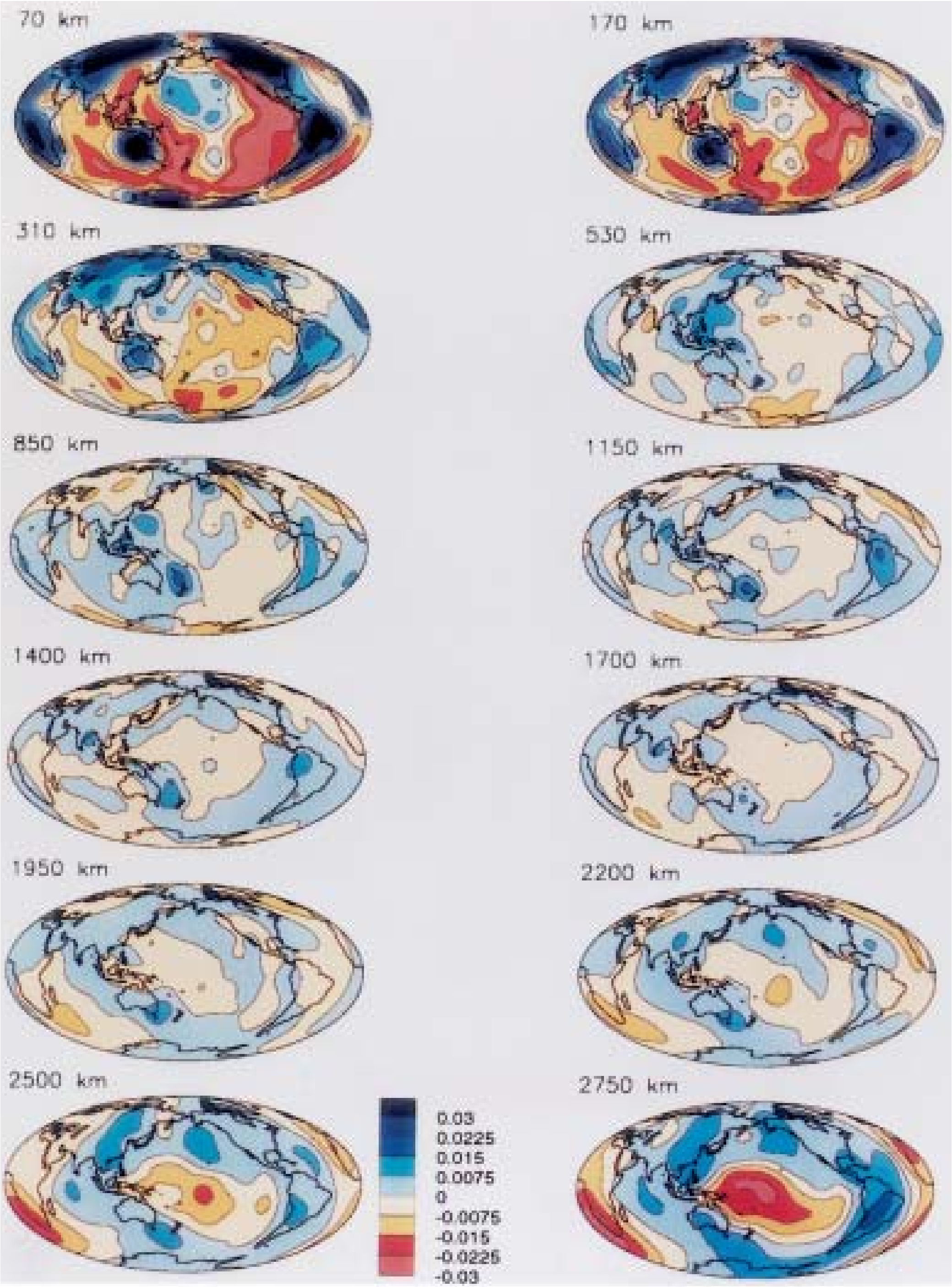

Figure 3.32. Perturbations in shear wave velocity V_S through the whole mantle at 12 depth slices, complete to spherical harmonic degree 16 determined by Masters et al. (1996).

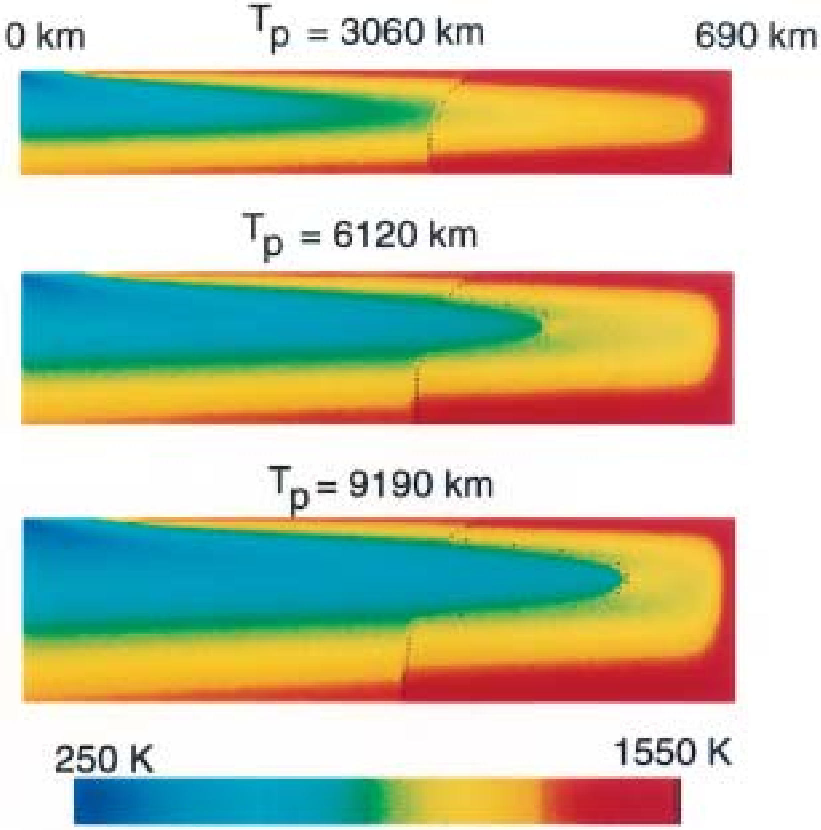

Figure 4.43. Temperature fields of three slabs with reaction rate-dependent olivine–spinel transformation. The slabs are shown horizontal but they dip 50° into the mantle. The horizontal coordinate is distance along the slab. The values of the thermal parameter T_p correspond to ages of 50, 100, and 150 Myr with $v = 80$ mm yr^{-1}. The dotted lines mark the isocontour corresponding to 99% completion of the phase change. After Devaux et al. (1997).